Temperature dependent load partitioning and slip mode transition in a eutectic AlCoCrFeNi<inf>2.1</inf> high entropy alloy

Materialia 17 (2021) 101118

Contents lists available at ScienceDirect

Materialia

journal homepage: www.elsevier.com/locate/mtla

Temperature dependent load partitioning and slip mode transition in a eutectic AlCoCrFeNi$_{2.1}$ high entropy alloy

Nitesh Raj Jaladurgam[a], Adrianna Lozinko[b], Sheng Guo[b], Tung-Lik Lee[c], Magnus Hörnqvist Colliander[a,*]

[a] Department of Physics, Chalmers University of Technology, Gothenburg SE-41296, Sweden
[b] Department of Industrial and Materials Science, Chalmers University of Technology, Gothenburg SE-41296, Sweden
[c] ISIS Neutron Facility, STFC Rutherford Appleton Laboratory, Harwell Campus, Didcot OX11 0QX, Oxfordshire, United Kingdom

ARTICLE INFO

Keywords:
Eutectic high entropy alloy
Neutron diffraction
Load distribution
Cube slip
Elastic lattice strains

ABSTRACT

Eutectic high entropy alloys are gaining increasing attention due to their excellent castability and combination of strength and ductility in the as-cast state. However, the detailed behavior of the nano-scale lamellar microstructure during deformation, and in particular the interaction between the phases, is not well understood. Here we use in-situ neutron diffraction during tensile testing over a wide temperature range (77–673 K) to obtain new insights into the temperature dependent mechanical interactions between and within phases during initial plastic deformation of an AlCoCrFeNi$_{2.1}$ eutectic high entropy alloy. The load was transferred from the L1$_2$ to the B2 phase during the yielding process, and the changing load distribution within the L1$_2$ phase with increasing temperature strongly suggests that $\langle 110 \rangle \{001\}$ cube slip is activated at room temperature and above. This points towards alloying design for delayed octahedral-to-cube slip transition as a possible strategy for increasing the high temperature strength of material.

1. Introduction

Since the introduction of the high entropy alloy (HEA) concept in 2004 [1,2], extensive efforts have been made to develop materials suitable for industrial applications in demanding environments. The vast majority of the work has been devoted to single phase alloys with either face centered cubic (FCC) or body centered cubic (BCC) crystal structures. While FCC HEAs typically show excellent ductility, they suffer from low strength [3,4]. The BCC structure, on the other hand, provides superior strength levels, but typically at the cost of much lowered ductility [5].

A new design strategy for improving the mechanical properties of HEAs, based on combining the principles of a eutectic microstructure with the high entropy alloy concept, lead to the development of *eutectic high entropy alloys* (EHEAs) [6]. Lu et al. [7] successfully developed an alloy AlCoCrFeNi$_{2.1}$ with excellent castability at industry scale with few defects. The eutectic microstructure consists of ordered L1$_2$ and ordered B2 phases [8,9], exhibiting Kurdjumov-Sachs (K-S) orientation relationship [10–12]. The complex lamellar microstructure with soft (L1$_2$) and hard (B2) phases contribute to an excellent combination of strength and ductility both at elevated [7] and cryogenic temperatures [13].

With respect to the origin of the mechanical properties of AlCoCrFeNi$_{2.1}$, micro-pillar compression of the individual phases in as-cast material showed that the B2 phase has a significantly higher critical resolved shear stress (CRSS), whereas L1$_2$ showed higher elastic stiffness [14]. Through nano-indentation testing, the strain rate sensitivity of the B2 phase was shown to be higher compared to L1$_2$, and very close to that observed from micro-indentation of the bulk alloy, suggesting that the deformation response is largely controlled by the hard B2 phase rather than the soft L1$_2$. Compression of bi-crystal micro-pillars containing both L1$_2$ and B2 showed that the L1$_2$ phase indeed yielded before B2, and that the interface remained intact without cracking or separation during the process, suggesting that the interphase boundaries have a strong influence on the resulting properties. The compliance of the interface could be explained by sliding through movement of screw-like partials on the FCC {111} interfacial planes, as suggested by molecular dynamics simulations of FCC/B2 composite materials with K-S orientation relationship by Choudhuri et al. [15].

Based on microstructural investigations of tensile tested specimens, Gao et al. [16] suggested that the lamellar structure lead to the creation of large back-stresses in the L1$_2$ phase due to extensive dislocation storage and pile-up at the interface between L1$_2$ and B2, which in turn promoted increased slip activity in B2. This was also confirmed by the simulations by Choudhari et al. [15], who demonstrated the occurrence of FCC-to-B2 slip transfer at the semi-coherent K-S interfaces, thereby allowing B2 to retain a stable flow stress during deformation. Such ef-

* Corresponding author.
E-mail address: magnus.colliander@chalmers.se (M. Hörnqvist Colliander).

https://doi.org/10.1016/j.mtla.2021.101118
Received 8 February 2021; Accepted 6 May 2021
Available online 18 May 2021

fects have also been observed during in-situ tensile testing in a transmission electron microscope (TEM), where the semi-coherent interfaces were suggested to increase the ability of B2 to deform plastically and thus avoid cracking of the otherwise typically brittle phase [10]. From the in-situ measurements it was also concluded that the $L1_2$ phase itself may contribute significantly to the strength of the alloy by extensive work hardening. The back-stress concept to describe the $L1_2$/B2 coupling effects on the strength and deformation behaviour of the eutectic microstructure was recently incorporated into a constitutive model by Wang et al. [17], which also indicated the strong influence of interfaces on the resulting macro-scale properties.

The complex interplay between the soft and hard phases and their interfaces clearly warrants further understanding of the progressive redistribution of the stress and strain between the phases during plastic deformation. In particular, such investigations should be performed on bulk specimens, rather than at the micro-scale, to retain the complex effects resulting from elastic interactions between the different phases and orientations. In the present work, we therefore use in-situ neutron diffraction during tensile testing of as-cast $AlCoCrFeNi_{2.1}$ at ambient conditions as well as cryogenic (77 K) and elevated (673 K) temperatures to study the development of phase-averaged and orientation-specific responses during the early stages of plastic deformation. In particular we could show how the load is transferred from the $L1_2$ phase to the B2 phase during yielding, and that there is a pronounced temperature induced change in the response of the $L1_2$ phase, which is proposed to be a result of the activation of dislocation slip on cube planes at room temperature and above. The outcomes of this study points towards alloy design for delayed octahedral-to-cube slip transition as a new strategy for increasing the high temperature strength, and can thereby benefit the future design and optimization of eutectic alloys.

2. Materials and methods

The EHEA was produced by vacuum induction melting of the elements in high purity Ar atmosphere to avoid contamination. The as-cast samples were machined for tensile tests with the gauge length and diameters of 40 mm and 8 mm, respectively. In-situ tensile tests were carried out at the time-of-flight (TOF) neutron diffractometer ENGIN-X, ISIS Neutron and Muon source, Rutherford Appleton Laboratory, UK. The tensile sample was loaded with the tensile axis inclined at 45° to the incident neutron beam. Two detectors are placed at $2\theta = \pm 90°$ to measure the lattice strains parallel and perpendicular to the tensile direction [18,19]. The chopper settings allowed recording of diffraction spectra covering a usable d-spacing range of 1–2.2 Å. Note that superlattice peaks were too weak to be observed in the in-situ diffractograms (see Fig. S1 in supplementary material for representative diffractograms), but the ordered $L1_2$ and B2 structures were confirmed by a dedicated neutron and electron diffraction experiments (see Results and Discussion section). Cryogenic tests were performed in vacuum using a dedicated testing chamber [20], whereas the room and elevated temperature tests were performed in air, the latter using a radiant furnace [21]. Acquisition were performed at constant load in the elastic regime, and subsequently in displacement control. To resolve the behaviour during elasto-plastic transition the density of data points was increased in the region corresponding to initial yielding, and the tests were stopped once fully plastic response had been achieved. Each diffraction pattern collection consumed about 20-30 minutes (after an initial waiting time of 5–10 min, depending on temperature, at each load/displacement level before starting the acquisition to allow for initial relaxation) with a gauge volume of $4 \times 4 \times 4$ mm^3 for all test conditions.

As-cast samples were sectioned along the axis corresponding to the tensile direction and prepared for imaging, chemical analysis using energy dispersive X-ray spectroscopy (EDS) and electron back-scatter diffraction (EBSD) in scanning electron microscopes (SEMs: TESCAN GAIA 3 and FEI Quanta 200). TEM investigations were performed at 200 keV acceleration voltage in an FEI Tecnai G20 to record the diffraction patterns of both phases.

Table 1
Average chemical composition of EHEA and the respective phases (in at. %) obtained from EDS.

Elements	Al	Co	Cr	Fe	Ni
Average	17.88	16.24	16.16	16.08	33.64
$L1_2$	10.58	18.43	20.72	19.43	30.83
B2	21.30	15.35	13.67	14.56	35.12

3. Results and discussion

3.1. Microstructure

The as-cast microstructure, as shown in Fig. 1(a), has a lamellar structure consisting of approximately 65 vol.% $L1_2$ (bright contrast) and 35 vol.% B2 (dark contrast). The SEM-EDS maps Fig. 1(b,c) confirms the previously reported element distribution in the individual phases [8,22], where Ni and Al enrich B2 and Fe, Co and Cr dominate the $L1_2$ phase. The average chemical composition measured using EDS is shown in Table. 1, together with the composition of the individual phases, which is in agreement with values reported in the literature [7,9,23]. Also, the previously observed K-S orientation relationship was confirmed, see Fig. 1(e) and (d), where the vast majority of the phase boundaries lay within 5° of the ideal orientation.

Fig. 2 (a) shows the neutron diffractograms obtained at room temperature with long counting time and chopper settings selected to cover larger d-spacings, where more superlattice peaks can be expected. Note that B2 peaks were clearly observed, whereas no signs of $L1_2$ superlattice peaks could be seen (Fig. 2(b,c)). However, the as-cast microstructure observed in TEM (Fig. 2(d,f)) revealed the presence of superlattice reflections in both phases, indicating the phases are indeed ordered $L1_2$ and ordered B2, which is consistent with the reported literature [22]. We also note the presence of nano-scale (around 20 nm) precipitates in the B2 phase (Fig. 2(e)). These has previously been shown to be Cr rich particles, coherent with the B2 matrix, which would have a strengthening effect by impeding dislocation motion [9,16]. However, as the particles are not observable in the diffractograms, we do not treat them further here. Instead their effects are indirectly included in the measured response of the B2 phase.

3.2. Macroscopic stress–strain response

The macroscopic stress-strain response (average stress from stress rig and strain calculated from compliance-corrected displacements during each neutron collection interval) at 77 K, 293 K and 673 K are shown in Fig. 3, including the approximate 0.1 % offset yield strengths, YS(0.1%). The flow curves follow the expected trends, with increasing stress levels as the temperature decreases from 673 K to 77 K. The stress-strain data was compared to literature [13] as well as separate ex-situ tests with material from a different batch and showed excellent agreement (see Fig. S2 in supplementary material). The full stress versus displacement curves and stress relaxation are shown in Fig. S3 in the supplementary material for reference. Note that the tensile test at 673 K took about 12 hours. This long duration might affect the microstructure, which in turn could affect the mechanical response. While good agreement was seen with ex-situ test performed at 673 K (see Fig. S2 in supplementary material) an un-deformed as-cast sample was heat treated separately for 12 hours at 673 K and the hardness was measured using micro-hardness (HV5g, average of 20 individual indents for each condition) before and after heat treatment in order to rule out such effects. Only a very small increase, from 292 ± 4 to 300 ± 3 HV5g (2.7%), could be observed, suggesting that the effect on microstructure due to long test duration at 673 K is negligible.

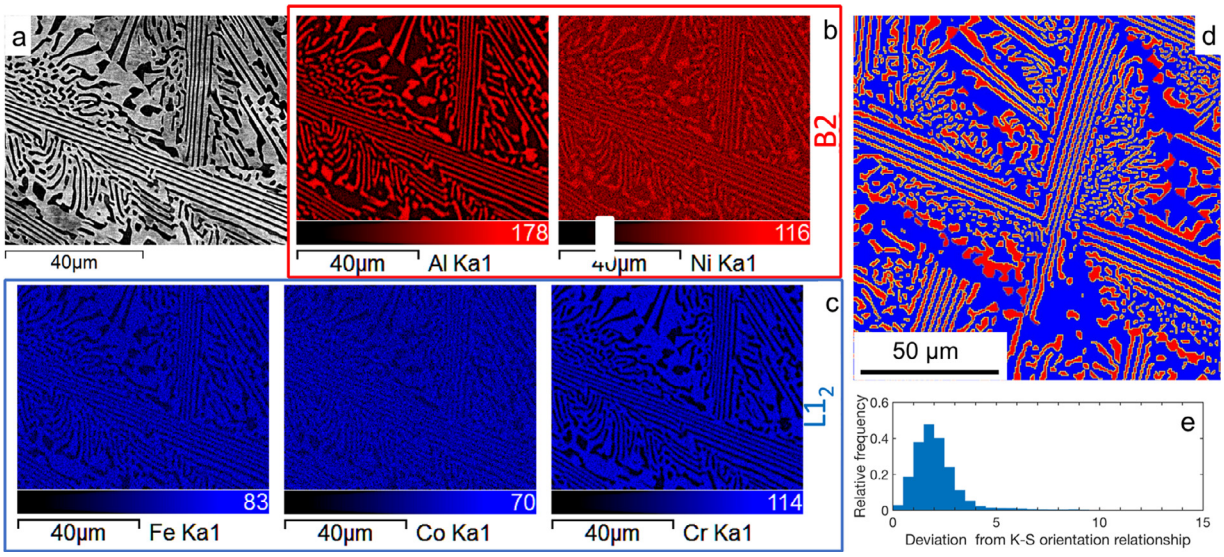

Fig. 1. (a) Eutectic structure along with EDS maps showing the rich contrast of (b) Ni and Al to B2, and (c) Fe,Co, Cr to $L1_2$. (d) The phase map shows $L1_2$ in red and B2 in blue. The yellow lines mark phase boundaries with less than 10° deviation from the Kurdjumov-Sachs (K-S) orientation relationship, and the actual distribution of deviations from K-S is shown in (e), respectively. (For interpretation of the references to colour in this figure legend, the reader is referred to the web version of this article.)

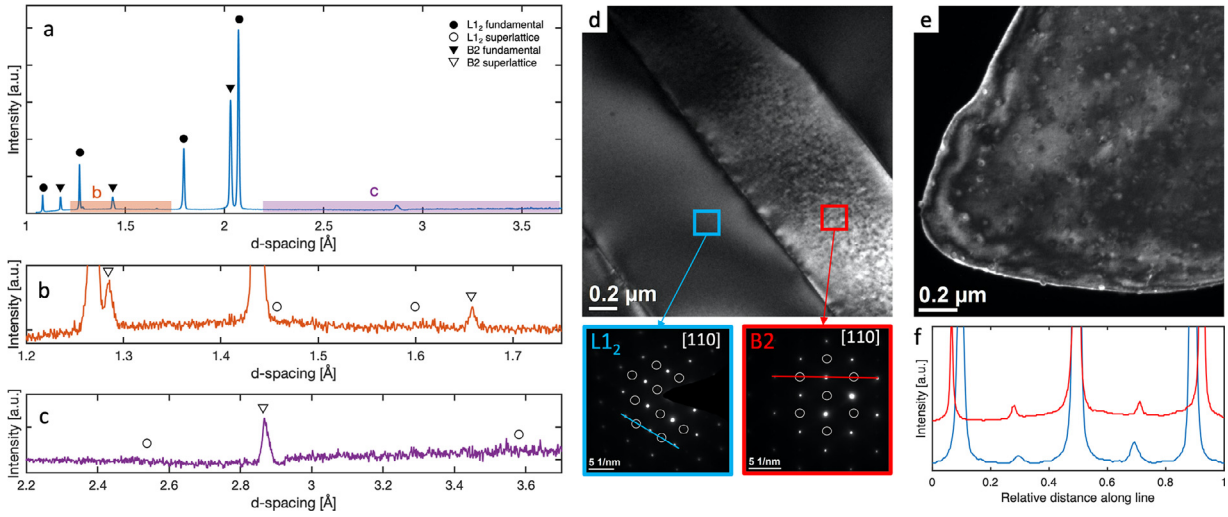

Fig. 2. (a)-(c) Neutron diffractogram obtained with long counting time and chopper setting selected to cover large d-spacings with access to more potential superlattice peaks. (a) Full diffractogram with filled circles and triangles indicate the positions of fundamental peaks form the $L1_2$ and B2 phases, respectively. (b) and (c) Magnified views of regions indicated in (a). Nominal positions of superlattice peaks for $L1_2$ and B2 are indicated by open circles and triangles, respectively. (d) The TEM micrograph of EHEA confirms the presence of ordered $L1_2$ and B2 phases from the corresponding SAED patterns (blue and red squares), obtained with zone axis [110]. (e) The particles in B2 are imaged in dark field. (f) The intensity variations of superlattice and fundamental spots are measured using a line drawn across the SAED patterns of $L1_2$ and B2. (For interpretation of the references to colour in this figure legend, the reader is referred to the web version of this article.)

3.3. Phase-averaged response

Fitting of the individual fundamental (*hkl*) peaks belonging to individual grain families (grains with the *hkl* direction parallel with the tensile axis) using GSAS-II [24] allowed extraction of *orientation-specific* lattice strain, i.e. the elastic strain in the corresponding grain family, in each phase (p) to be calculated as $\epsilon_p^{hkl} = d_p^{hkl}/d_{p,0}^{hkl} - 1$, where $d_{p,0}^{hkl}$ is the un-strained lattice parameter (here taken from the fits obtained at zero load, thus neglecting any initial internal stresses). The *phase-averaged* elastic strains, ϵ_p, were subsequently calculated as the multiplicity-weighted average of the individual grain families [25]. The phase-averaged lattice strains against applied stress are shown in Fig. 4.

Note that the phase-averaged lattice strains in the transverse direction could not be calculated for the B2 phase at 293 K. The reason is the absence of the (200) peak (see Fig. S1(b2) in the supplementary material), presumably due to unfortunate orientation of the specimen in the stress rig. As will be shown later, the (200) oriented grains behave distinctly different from other orientations in the B2 phase, and the absence of this peak therefore prevents reliable calculation of the phase-averaged strains. The $L1_2$ phase yields well before YS(0.1%) is reached, and after yielding the elastic lattice strains in $L1_2$ remain approximately constant, which indicates that plastic deformation with very limited work hardening occurs. The load is instead transferred to B2, where the increasing lattice strains indicates that the phase carries much higher loads compared to $L1_2$ (as the phase-averaged stress is proportional to the phase-averaged elastic strain). Although the present measurements were not optimized for extraction of the elastic properties (with only three to four points being in the elastic region), approximate values of

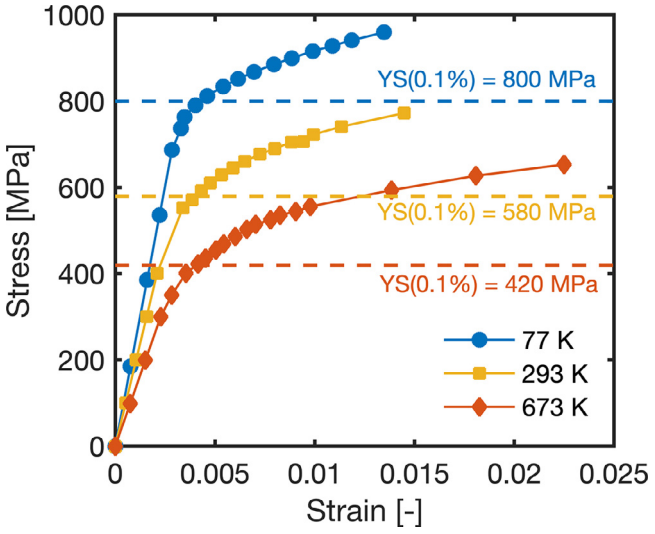

Fig. 3. Macroscopic stress–strain curves measured at 77 K, 293 K and 673 K. Dashed lines indicate the 0.1% offset yield strengths.

the phase-averaged modulii can be extracted by a linear fit to the macroscopic stress–phase-averaged lattice strain data before yielding. At room temperature, we find $E^{293K}_{L1_2} = 210$ GPa and $E^{293K}_{B2} = 193$ GPa, in good agreement with Muskeri et al. who reported values of 216 GPa for the $L1_2$ phase and 180 GPa for B2 [14]. At 77 K, we find $E^{77K}_{L1_2} = 238$ GPa and $E^{77K}_{B2} = 219$ GPa, and at 673 K $E^{673K}_{L1_2} = 149$ GPa and $E^{673K}_{B2} = 141$ GPa. Based on the measured phase-specific strains and modulii, phase-averaged stresses can be calculated as

$$\sigma_p = \frac{E_p}{(1+\nu_p)(1-2\nu_p)}\left[(1-\nu_p)\epsilon^a_p + 2\nu_p\epsilon^{tr}_p\right] \quad (1)$$

where ϵ^a_p and ϵ^{tr}_p are the phase-averaged elastic strains in the axial (tensile) and transverse direction, respectively, and ν_p is Poisson's ratio. As the quality of the data in the transverse direction was not sufficient to allow reliable determination of ν for the different phases we assume $\nu_{L1_2} = \nu_{B2} = 0.3$, which does not significantly affect the results (see Fig. S4 and discussion in supplementary material). Due to the absence of phase-averaged transverse elastic strains for the B2 phase at 293 K, Eq. (1) could not be used. Instead, for this particular case *approximate* stresses where calculated as $\bar{\sigma}^{77K}_{B2} = E^{a,77K}_{B2}\epsilon^{77K}_{B2}$ (Eq. 2). The difference between the approximate stresses and the stresses calculated by Eq. (1) was checked for the other cases, and the error was found to be negligible (see supplementary material, Fig. S5). Consequently, the approximate stresses were used for the B2 phase at 293 K.

The phase-averaged stress of $L1_2$ and B2 are plotted against the macroscopic strain along with the stress–strain curve in Fig. 4(d–f). Very high stresses (exceeding 2 GPa at 77 K) in the B2 phase are clearly observed, whereas $L1_2$ behaves almost perfectly plastic for all temperatures, which appears to contradict the suggested effect of extensive strain hardening of this phase on the macroscopic response [10]. However, Wang et al. [10] used cold rolling to larger strains to demonstrate the hardening effect, whereas our observations are limited to small strains in tension. Also included in Fig. 4(d–f) is the average stress according to the rule-of-mixture (ROM) $\bar{\sigma} = v_f\sigma_{B2} + (1-v_f)\sigma_{L1_2}$, where $v_f = 0.35$ is the volume fraction of B2 according the EBSD measurement. The macroscopic stress–strain curves agree reasonably well with the average stress, but, particularly at 77 K, falls closer to the response of the $L1_2$ phase. This is not surprising, as the softer $L1_2$ is the continuous phase, but is nevertheless in contrast to the previously suggested B2 dominance on the bulk response derived from indentation measure-

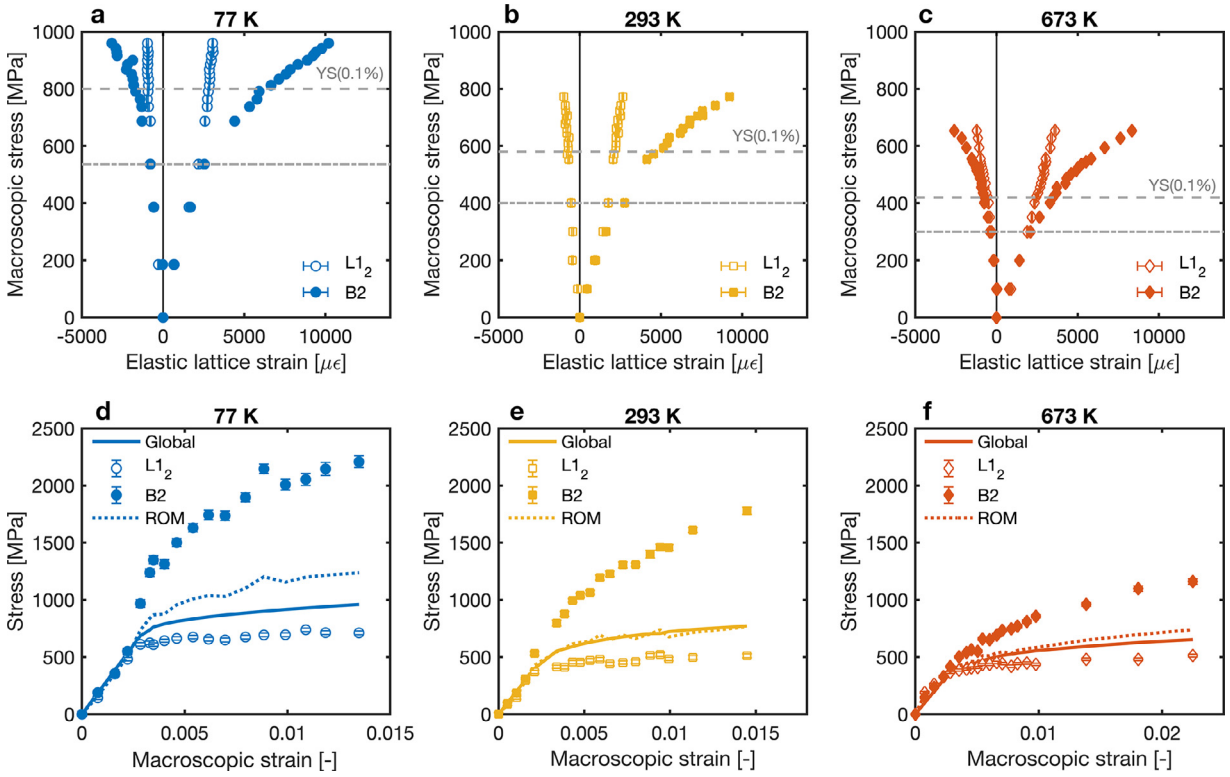

Fig. 4. Phase-averaged lattice strain (a-c) and stress (d-f) response measured at (a,d) 77 K, (b,e) 293 K and (c,f) 673 K. Note the absence of transverse strains for the B2 phase at 293 K (see text for more details). Dashed lines in (a)-(c) indicate YS(0.1%), whereas dash-dotted lines indicate the data point where distinct load transfer is first observed. Dotted lines in (d)e-(e) indicate average stresses calculated from the rule-of-mixtures (ROM).

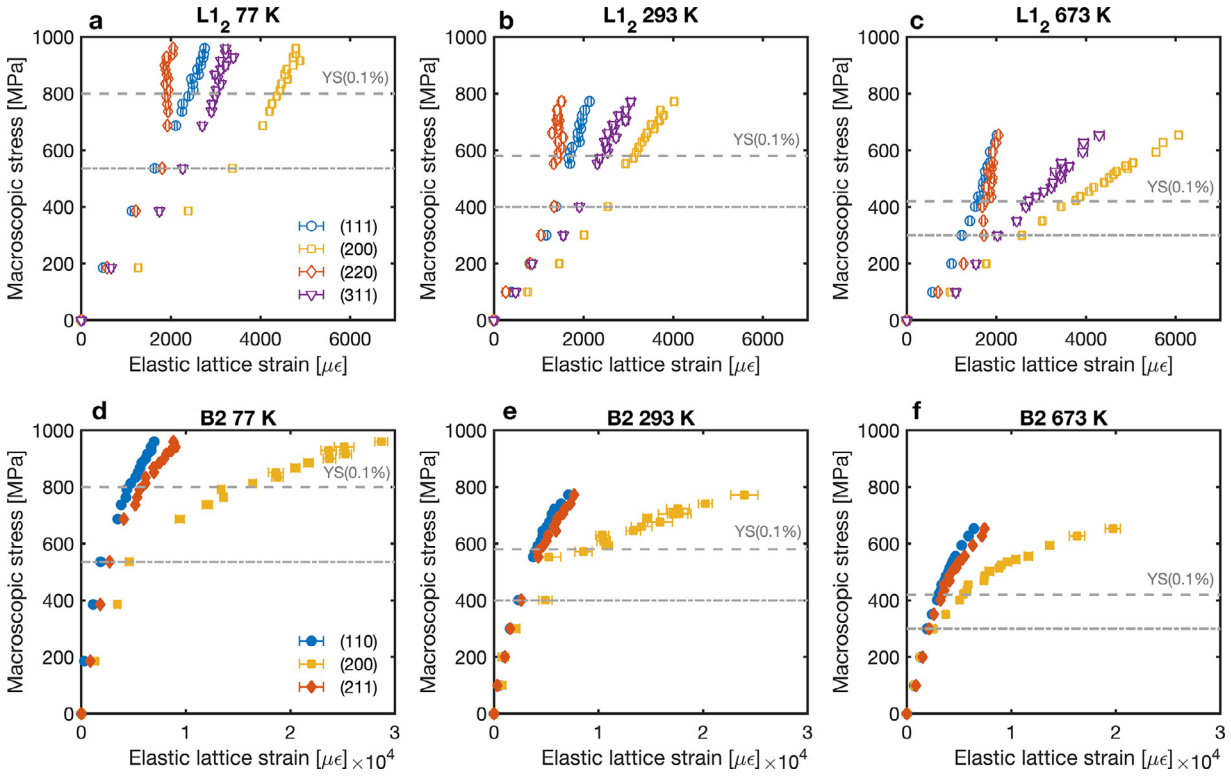

Fig. 5. Elastic lattice strains from fundamental peaks for $L1_2$ (a-c) and B2 (d-f) at 77 K (a,d), 293 K (b,e) and 673 K (c,f), respectively. Dashed lines indicate YS(0.1%), whereas dash-dotted lines indicate the data point where distinct load transfer is first observed.

ments [14]. Here, we also note a difference in the temperature dependence of the phase-averaged response of the phases. The B2 phase shows drastically decreasing stress levels with increasing temperature, whereas the phase-averaged stress in the $L1_2$ phase decrease between 77 K and 293 K, but then remains at similar levels at 673 K.

3.4. Orientation-specific response

Fig. 5 shows the evolution of orientation-specific lattice strains derived from four fundamental peaks of $L1_2$ and three fundamental peaks of B2 (the strains of the (220) peak was also measured but not included in Fig. 5 in order to increase the readability of the figure, as it almost completely overlapped with (110), as expected). The difference in slope of lattice strains in the elastic regime strongly indicates the presence of elastic anisotropy in $L1_2$. After yielding at 77 K (Fig. 5(a)), grains with the (220) planes perpendicular to the loading direction yield first, and deform without significant work hardening. The remaining orientations behave almost linear, with only a slight upward bending after yielding, indicating work hardening. The behaviour is similar at room temperature, Fig. 5(b), but we also notice that the (200) and (311) orientations start to bend towards larger lattice strains at higher stresses. At 673 K, the behaviour of (220) is similar to lower temperatures (77 K and 293 K), with early yielding and no work hardening, but the response of the other orientation changes drastically, see Fig. 5(c). The (200) and (311) orientated grains of $L1_2$ now deviate more significantly towards larger lattice strains, and the first stage (small upward deviations) is absent. Even more pronounced is the very early yielding of (111), which appears to deform plastically even before (220).

Here, it should be noted that the diffraction data was collected at constant displacement in the plastic region, which could allow stress relaxation to occur. However, the examination of the load - time data from the stress rig showed that the relaxation at the last few data points (highest stresses) at 673 K translates to changes in elastic strains in the order of 150 $\mu\epsilon$ during data acquisition, and much smaller values at lower stresses and temperatures (see supplementary material Fig. S3). Viscous effects are therefore not expected to be the cause of the change in behaviour at 673 K. We also note that the plastic strains were too small to allow detectable changes in peak width and intensity, so deformation induced texture evolution will not affect the results. Instead, the changes in lattice strain response in $L1_2$ at 673 K (earlier yielding in (111) oriented grains compared to (220)) strongly indicates a change in dominating deformation mechanism compared to lower temperatures.

While the behavior at 77 K and 293 K are consistent with $\langle 110 \rangle \{111\}$ octahedral slip, early yielding of the (111) orientation could be explained by the occurrence of slip on the favourably oriented $\{001\}$ cube planes. Cube slip on $\langle 110 \rangle \{001\}$ systems is well known to occur in $L1_2$ single crystals above a critical temperature, in particular when loaded along the $\langle 111 \rangle$ direction [26–29]. The effect of cube slip on the response of the $L1_2$ phase is even more clear in the approximate orientation-specific axial stress evolution ($\bar{\sigma}^{hkl}_{L1_2} = E^{hkl}_{L1_2} \epsilon^{hkl}_{L1_2}$) shown in Fig. 6 (the contribution from the transverse interaction stresses were neglected due to insufficient data quality in the transverse direction and the extra degree of freedom of the grain orientations). At 77 K (Fig. 6(a)), where octahedral slip prevails, the (111) oriented grains, which are unfavourably oriented for slip activation (high maximum Schmid factor in Table 2) are subjected to high stresses, whereas near-ideal plastic behaviour is observed in the (220) oriented grains and intermediate response is seen in (200) and (311). While, the Schmid factor for octahedral slip is actually identical for (200) and (220) (Table 2), the lower elastic stiffness leads to lower resolved shear stresses for (200) oriented grains, and hence less slip activation.

At room temperature (Fig. 6(b)), on the other hand, the stress in the (111) oriented grains is similar to (200) and (311) orientations, indicating that cube slip is likely activated already at this temperature. The critical temperature depends on the alloy chemistry, but many systems have been shown to undergo cube slip at room temperature [29,30], or even below [30], when deformed in the $\langle 111 \rangle$ direction. While cube slip has a large effect on the response of the (111) grains, due to the

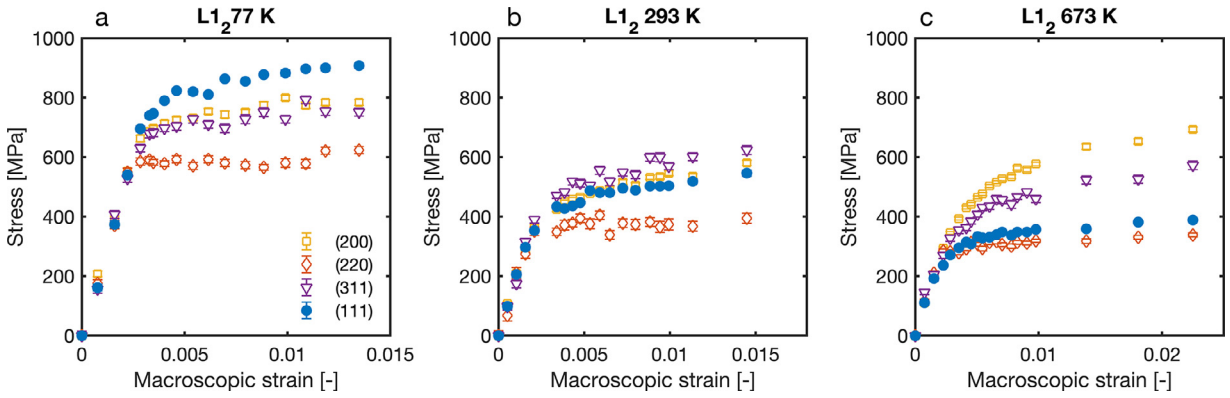

Fig. 6. Orientation-specific stress in different $L1_2$ grain families as a function of macroscopic strain.

Table 2
Maximum Schmid factors on $\langle 110\rangle\{001\}$ cube (m^{cube}_{max}) and $\langle 110\rangle\{111\}$ octahedral (m^{oct}_{max}) slip systems in grain families with different tensile axes. N^{cube}_{max} and N^{oct}_{max} are the number of independent system experiencing the maximum Schmid factor for cube and octahedral slip, respectively.

Tensile axis	m^{cube}_{max}	N^{cube}_{max}	m^{oct}_{max}	N^{oct}_{max}	$m^{cube}_{max}/m^{oct}_{max}$
(111)	0.4714	3	0.2722	6	1.73
(200)	0	–	0.4082	8	0
(220)	0.3536	4	0.4082	4	0.86
(311)	0.3857	1	0.4454	2	0.86

very high Schmid factor compared to octahedral slip systems, the effect is negligible in (220) and (311) grains, as the Schmid factor for cube slip in these grains are lower than for octahedral slip (Table 2), and the CRSS is likely higher due to a smaller interplanar spacing.

Finally, at 673 K (Fig. 6(c)), extensive activation of cube slip leads to low stresses in the (111) grains, but here also a lowering of stresses in the (311) grains can be observed. The occurrence of cube slip is primarily related to the increased mobility of $\langle 110\rangle$ dislocations on the $\{001\}$ plane as thermal activation allows recombination of the partials involved in the non-planar dissociation [31], and the anomalous temperature dependence of the octahedral slip systems [26]. As the CRSS for slip on $\langle 110\rangle\{001\}$ has been shown to have a large positive strain rate sensitivity [27], the combination of increased temperature, low deformation rate and dwell time during neutron diffraction measurements could be expected to promote the activation of cube slip also in the (311) oriented grains. Consistent with the suggested transition to cube slip, the (200) orientation appears to be unaffected as the Schmid factor for cube slip is zero (Table 2). As the octahedral-to-cube slip transition is known to reverse the anomalous temperature dependence of the strength of $L1_2$, the observation of cube slip in the EHEA could point towards alloy design for delaying this transition as a possible strategy for further increasing the strength at elevated temperatures. We also note that as the temperature range covered by the present investigation contains the entire transition from octahedral to cube slip it offers the possibility to calibrate and use crystal plasticity models, either finite element based or self-consistent, in order to more fully explore the transition. Such simulations would for example allow estimation of the CRSS and relative slip activity of the different slip systems, as well as effects on e.g. latent hardening.

Contrary to $L1_2$, the elastic response of B2 is approximately isotropic in the elastic region (Fig. 5(d-f)). Furthermore, load redistribution response in B2 is similar at all temperatures. The evolution of lattice strains in the (110) and (211) orientations follow each other closely, showing only small deviations towards larger strains, whereas the (200) orientation accommodates very large elastic lattice strains, i.e. carries the majority of the load. Load transfer to (200) orientation within FCC is commonly observed in e.g. austenitic/ferritic duplex steels [32,33], but not to the extreme levels observed here. At the end of the 673 K test, the (200) lattice strain is in the order of 2 %, corresponding to stress levels around 3 GPa. Wollmershauser et al. [34] examined the evolution of lattice strains during deformation of several single-phase B2 alloys (including NiAl) in compression, and observed very similar behaviour, with very large lattice strains in (200) oriented grains. Furthermore, the pronounced K-S orientation relationship could play a role through the $L1_2$-to-B2 load transfer process, which remains to be investigated.

4. Conclusions

In summary, in-situ neutron diffraction during uniaxial tensile tests were performed on newly developed EHEA at 77 K, 293 K and 673 K, in order to understand the load distribution between and within the ordered $L1_2$ and B2 phases. The phase-averaged lattice strains were found to indicate a distinct load transfer from $L1_2$ to B2 at all three measured temperatures. The B2 phase behaved similar over the entire temperature range, with the (200) direction carrying most of the load, whereas a detailed investigation of the orientation-specific response of the $L1_2$ phase indicates that cube slip becomes predominant at higher temperatures, in particular in grains loaded in the $\langle 111\rangle$ direction. The load distribution within the eutectic microstructure, and in particular the suggested activation of cube slip in $L1_2$ already at room temperature, significantly increases our understanding of the deformation of this promising class of alloys, and paves the way for further alloy development to optimise the high temperature properties, as well as development of accurate crystal plasticity models to describe the mechanical response.

Declaration of Competing Interest

No potential conflict of interest was reported by the authors.

Acknowledgements

Authors are grateful to ISIS Neutron and Muon source, UK, for the beamtime (RB1720280) at Engin-X. The work was performed in part at the Chalmers Materials Analysis Laboratory CMAL. Authors are grateful to Prof. Yiping Lu from School of Materials Science and Engineering, Dalian University of Technology, China for providing the EHEA material for this work. Prof. Christer Persson at Chalmers University of Technology is acknowledged for providing access to mechanical testing facilities for the ex-situ tests. This research is funded by the Swedish Foundation for Strategic Research (SSF) within the Swedish National Graduate School in Neutron Scattering (SwedNESS) with Grant number GSn15-0008.

Supplementary material

Supplementary material associated with this article can be found, in the online version, at10.1016/j.mtla.2021.101118

References

[1] J.W. Yeh, S.K. Chen, S.J. Lin, J.Y. Gan, T.S. Chin, T.T. Shun, C.H. Tsau, S.Y. Chang, Nanostructured high-entropy alloys with multiple principal elements: novel alloy design concepts and outcomes, Adv. Eng. Mater. 6 (5) (2004) 299–303, doi:10.1002/adem.200300567.

[2] B. Cantor, I.T.H. Chang, P. Knight, A.J.B. Vincent, Microstructural development in equiatomic multicomponent alloys, Mater. Sci. Eng. A 375–377 (1–2 SPEC. ISS.) (2004) 213–218, doi:10.1016/j.msea.2003.10.257.

[3] F. Wang, Y. Zhang, G. Chen, H.A. Davies, Tensile and compressive mechanical behavior of a cocrcufenial 0.5 high entropy alloy, Int. J. Modern Phys. B 23 (06n07) (2009) 1254–1259, doi:10.1142/S0217979209060774.

[4] F. Otto, A. Dlouhý, C. Somsen, H. Bei, G. Eggeler, E.P. George, The influences of temperature and microstructure on the tensile properties of a CoCrFeMnNi high-entropy alloy, Acta Mater. 61 (15) (2013) 5743–5755, doi:10.1016/j.actamat.2013.06.018.

[5] O.N. Senkov, G.B. Wilks, D.B. Miracle, C.P. Chuang, P.K. Liaw, Refractory high-entropy alloys, Intermetallics 18 (9) (2010) 1758–1765, doi:10.1016/j.intermet.2010.05.014.

[6] Y. Lu, Y. Dong, H. Jiang, Z. Wang, Z. Cao, S. Guo, T. Wang, T. Li, P.K. Liaw, Promising properties and future trend of eutectic high entropy alloys, Scr. Mater. 187 (2020) 202–209, doi:10.1016/j.scriptamat.2020.06.022.

[7] Y. Lu, Y. Dong, S. Guo, L. Jiang, H. Kang, T. Wang, B. Wen, Z. Wang, J. Jie, Z. Cao, H. Ruan, T. Li, A promising new class of high-temperature alloys: eutectic high-entropy alloys, Sci. Rep. 4 (1) (2014) 6200, doi:10.1038/srep06200.

[8] I.S. Wani, T. Bhattacharjee, S. Sheikh, Y.P. Lu, S. Chatterjee, P.P. Bhattacharjee, S. Guo, N. Tsuji, Ultrafine-grained AlCoCrFeNi 2.1 eutectic high-entropy alloy, Mater. Res. Lett. 4 (3) (2016) 174–179, doi:10.1080/21663831.2016.1160451.

[9] I. Wani, T. Bhattacharjee, S. Sheikh, P.P. Bhattacharjee, S. Guo, N. Tsuji, Tailoring nanostructures and mechanical properties of $AlCoCrFeNi_{2.1}$ eutectic high entropy alloy using thermo-mechanical processing, Mater. Sci. Eng. 675 (2016) 99–109, doi:10.1016/j.msea.2016.08.048.

[10] Q. Wang, Y. Lu, Q. Yu, Z. Zhang, The exceptional strong face-centered cubic phase and semi-coherent phase boundary in a eutectic dual-phase high entropy alloy AlCoCrFeNi, Sci. Rep. 8 (1) (2018) 1–7, doi:10.1038/s41598-018-33330-0.

[11] A. Lozinko, O.V. Mishin, T. Yu, U. Klement, S. Guo, Y. Zhang, Quantification of microstructure in a eutectic high entropy alloy AlCoCrFeNi 2.1, IOP Conf. Ser. 580 (2019) 012039, doi:10.1088/1757-899X/580/1/012039.

[12] A. Lozinko, Y. Zhang, O.V. Mishin, U. Klement, S. Guo, Microstructural characterization of eutectic and near-eutectic AlCoCrFeNi high-entropy alloys, J. Alloy. Compd. 822 (2020) 153558, doi:10.1016/j.jallcom.2019.153558.

[13] T. Bhattacharjee, R. Zheng, Y. Chong, S. Sheikh, S. Guo, I.T. Clark, T. Okawa, I.S. Wani, P.P. Bhattacharjee, A. Shibata, N. Tsuji, Effect of low temperature on tensile properties of AlCoCrFeNi 2.1 eutectic high entropy alloy, Mater. Chem. Phys. (2017) 1–6, doi:10.1016/j.matchemphys.2017.06.023.

[14] S. Muskeri, V. Hasannaeimi, R. Salloom, M. Sadeghilaridjani, S. Mukherjee, Small-scale mechanical behavior of a eutectic high entropy alloy, Sci. Rep. 10 (1) (2020) 1–12, doi:10.1038/s41598-020-59513-2.

[15] D. Choudhuri, S.G. Srinivasan, R.S. Mishra, Deformation of lamellar FCC-B2 nanostructures containing Kurdjumov-Sachs interfaces: relation between interfacial structure and plasticity, Int. J. Plast. 125 (2020) 191–209, doi:10.1016/j.ijplas.2019.09.014.

[16] X. Gao, Y. Lu, B. Zhang, N. Liang, G. Wu, G. Sha, J. Liu, Y. Zhao, Microstructural origins of high strength and high ductility in an AlCoCrFeNi2.1 eutectic high-entropy alloy, Acta Mater. 141 (2017) 59–66, doi:10.1016/j.actamat.2017.07.041.

[17] Y. Wang, W. Chen, J. Zhang, J. Zhou, A quantitative understanding on the mechanical behavior of AlCoCrFeNi2.1 eutectic high-entropy alloy, J. Alloy. Compd. 850 (2021) 156610, doi:10.1016/j.jallcom.2020.156610.

[18] J.R. Santisteban, M.R. Daymond, J.A. James, L. Edwards, ENGIN-X: a third-generation neutron strain scanner, J. Appl. Crystallogr. 39 (2006) 812–825, doi:10.1107/S0021889806042245.

[19] B.M.B. Grant, E.M. Francis, J. Quinta Da Fonseca, M.R. Daymond, M. Preuss, Deformation behaviour of an advanced nickel-based superalloy studied by neutron diffraction and electron microscopy, Acta Mater. 60 (2012) 6829–6841, doi:10.1016/j.actamat.2012.09.005.

[20] O. Kirichek, J.D. Timms, J.F. Kelleher, R.B. Down, C.D. Offer, S. Kabra, S.Y. Zhang, Sample environment for neutron scattering measurements of internal stresses in engineering materials in the temperature range of 6 K to 300 K, Rev. Sci. Instrum. 88 (2) (2017) 025103, doi:10.1063/1.4974815.

[21] R. Haynes, A. Paradowska, M. Chowdhury, C. Goodway, R. Done, O. Kirichek, E. Oliver, An inert-gas furnace for neutron scattering measurements of internal stresses in engineering materials, Meas. Sci. Technol. 23 (4) (2012) 047002, doi:10.1088/0957-0233/23/4/047002.

[22] Y. Zhang, X. Wang, J. Li, Y. Huang, Y. Lu, X. Sun, Deformation mechanism during high-temperature tensile test in an eutectic high-entropy alloy AlCoCrFeNi2.1, Mater. Sci. Eng. A 724 (2018) 148–155, doi:10.1016/j.msea.2018.03.078.

[23] T. Bhattacharjee, R. Zheng, Y. Chong, S. Sheikh, S. Guo, I.T. Clark, T. Okawa, I.S. Wani, P.P. Bhattacharjee, A. Shibata, et al., Effect of low temperature on tensile properties of AlCoCrFeNi2.1 eutectic high entropy alloy, Mater. Chem. Phys. 210 (2018) 207–212, doi:10.1016/j.matchemphys.2017.06.023.

[24] B.H. Toby, R.B. Von Dreele, IUCr, GSAS-II: the genesis of a modern open-source all purpose crystallography software package, J. Appl. Crystallogr. 46 (2) (2013) 544–549, doi:10.1107/S0021889813003531.

[25] M.R. Daymond, The determination of a continuum mechanics equivalent elastic strain from the analysis of multiple diffraction peaks, J. Appl. Phys. 96 (8) (2004) 4263–4272, doi:10.1063/1.1794896.

[26] A.E. Staton-Bevan, R.D. Rawlings, The deformation behaviour of single crystal Ni_3(Al, Ti), Phys. Status Solidi 29 (1975) 613–622, doi:10.1002/pssa.2210290232.

[27] Y. Umakoshi, D.P. Pope, V. Vitek, The asymmetry of the flow stress in Ni_3(Al,Ta) single crystals, Acta Metall. 32 (1984) 449–456, doi:10.1016/0001-6160(84)90118-4.

[28] T. Saburi, T. Hamana, S. Nenno, H.-r. Pak, Temperature and orientation dependence of the yield strength of Ni_3(Al, W), Jpn. J. Appl. Phys. 16 (1977) 267–272, doi:10.1143/JJAP.16.267.

[29] C. Lall, S. Chin, D.P. Pope, The orientation and temperature dependence of the yield stress of Ni_3(Al, Nb) single crystals, Metall. Trans. A 10 (1979) 1323–1332, doi:10.1007/BF02811988.

[30] N. Clément, A. Couret, D. Caillard, An in situ study of cube glide in the γ'-phase of a superalloy, Philos. Mag. A 64 (1991) 669–695, doi:10.1080/01418619108204867.

[31] Y. Sun, P. Hazzledine, Chapter 49 geometry of dislocation glide in $L1_2\gamma'$-phase: TEM observations, in: F. Nabarro, M. Duesbury (Eds.), Dislocations in Solids, 10, Elsevier, 1996, pp. 27–68, doi:10.1016/S1572-4859(96)80004-0.

[32] N. Jia, R. Lin Peng, D.W. Brown, B. Clausen, Y.D. Wang, Tensile deformation behavior of duplex stainless steel studied by in-situ time-of-flight neutron diffraction, Metall. Mater. Trans. A 39 (13) (2008) 3134–3140, doi:10.1007/s11661-008-9675-2.

[33] A. Baczmański, Y. Zhao, E. Gadalińska, L. Le Joncour, S. Wroński, C. Braham, B. Panicaud, M. François, T. Buslaps, K. Soloducha, Elastoplastic deformation and damage process in duplex stainless steels studied using synchrotron and neutron diffractions in comparison with a self-consistent model, Int. J. Plast. 81 (2016) 102–122, doi:10.1016/j.ijplas.2016.01.018.

[34] J.A. Wollmershauser, S. Kabra, S.R. Agnew, In situ neutron diffraction study of the plastic deformation mechanisms of B2 ordered intermetallic alloys: NiAl, CuZn, and CeAg, Acta Mater. 57 (1) (2009) 213–223, doi:10.1016/j.actamat.2008.08.066.